Dryline Bulge Evolution in a Two-Dimensional Mixed-Layer Model

GLENN M. AUSLANDER AND PETER R. BANNON

Department of Meteorology, The Pennsylvania State University, University Park, Pennsylvania

(Manuscript received 1 August 2003, in final form 26 May 2004)

ABSTRACT

This study examines the diurnal response of a mixed-layer model of the dryline system to localized anomalies of surface heat flux, topography, mixed-layer depth, and inversion strength. The two-dimensional, mixed-layer model is used to simulate the dynamics of a cool, moist layer east of the dryline capped by an inversion under synoptically quiescent conditions. The modeled domain simulates the sloping topography of the U.S. Great Plains. The importance of this study can be related to dryline bulges that are areas with enhanced convergence that may trigger convection in suitable environmental conditions.

All anomalies are represented by a Gaussian function in the horizontal whose amplitude, size, and orientation can be altered. A positive, surface-heat-flux anomaly produces increased mixing that creates a bulge toward the east, while a negative anomaly produces a westward bulge. Anomalies in topography show a similar trend in bulge direction with a peak giving an eastward bulge, and a valley giving a westward bulge. Anomalies in the initial mixed-layer depth yield an eastward bulge in the presence of a minimum and a westward bulge for a maximum. An anomaly in the initial inversion strength results in a westward bulge when the inversion is stronger, and an eastward bulge when the inversion is weak. The bulges observed in this study at 1800 LT ranged from 400 to 600 km along the dryline and from 25 to 80 km across the dryline.

When the heating ceases at night, the entrainment and eastward movement of the line stops, and the line surges westward. This westward surge at night has little dependence on the type of anomaly applied. Whether a westward or eastward bulge was present at 1800 LT, the surge travels an equal distance toward the west. However, the inclusion of weak nocturnal friction reduces the westward surge by 100 to 200 km due to mechanical mixing of the very shallow leading edge of the surge.

All model runs exhibit peaks in the mixed-layer depth along the dryline at 1800 LT caused by enhanced boundary layer convergence and entrainment of elevated mixed-layer air into the mixed layer. These peaks appear along the section of the dryline that is least parallel to the southerly flow. They vary in amplitude from 4 to 9 km depending on the amplitude of the anomaly. However, the surface-heat-flux anomalies generally result in peaks at the higher end of this interval. It is hypothesized that the formation of these peaks may be the trigger for deep convection along the dryline in the late afternoon.

1. Introduction

Quiescent drylines are usually found in the U.S. Great Plains during the spring. Their movement is important to study for the initiation of convection. Schaefer (1974a,b) and Miller et al. (2001) review the basic features of the dryline. The dryline is a surface boundary that separates different air masses; a relatively cool, moist air mass originates from the Gulf of Mexico via a southerly low-level flow, and a warm, dry air mass originates from the high-altitude plateaus in the desert Southwest. Warm, dry air aloft caps the moist air to the east to create an inversion that is referred to as the dry front (Fujita 1958). The intersection of the dry front with the topography, which slopes upward to the west, is known as the dryline. The dryline exhibits daytime movement eastward as the slope of the dry front becomes steeper. The dryline undergoes westward retrogression at night as the dry front slope lessens and winds associated with a low-level jet increase to a maximum near midnight.

Dryline bulges are areas along the dryline whose movement relative to the rest of the dryline is altered, and they focus convergence for increased convective activity (Schaefer 1986b). Surface winds tend to deviate near the bulge to match those of the winds aloft. Schaefer (1986a) speculated that dryline bulges are created by mid- to upper-tropospheric jets that force subsidence aloft. Through turbulent mixing, this dry air is transported to the surface to the west of the dryline. Koch (1979) hypothesized that bulges form as a result of locally enhanced westerly momentum mixing to the surface to the west of the dryline. A later study (McCarthy and Koch 1982) attributed dryline motion to mesoscale wave propagation northward along the dryline. These waves are similar to the bulges in this study, but have

Corresponding author address: Peter R. Bannon, Dept. of Meteorology, The Pennsylvania State University, University Park, PA 16802.
E-mail: bannon@ems.psu.edu

smaller dimensions They found that these waves were present when the dryline motion is toward the east, but were no longer observed when dryline movement to the east ceased.

Other factors that may be important for dryline bulge formation are surface heterogeneities, such as variability in the surface heat flux and topography. Incoming solar radiation impinging on different land surfaces may lead to different surface heat fluxes. Land surfaces with high vegetation densities contribute more toward latent heat flux than sensible heat flux. On the other hand, barren regions that are dry have a greater contribution to sensible heat flux than latent heat flux. Cloud cover (e.g., McNider and Kopp 1990) may also play a role in altering surface heat flux. Land surfaces under a persistent cloud deck will have a smaller sensible heat flux. Therefore, both heat and moisture flux variability may contribute to variations in turbulent mixing and dryline bulge formation. Previous studies (Grasso 2000; Ziegler et al. 1995; Shaw et al. 1997) using numerical mesoscale models to investigate the effects of soil moisture on the dryline have shown that horizontal moisture variations are important for dryline morphology through their effect on surface heat fluxes. A lack of moisture variability may even prevent dryline formation (Ziegler et al. 1995). Topography also can play a role in dryline motion (Peckham and Wicker 2000). Schaefer (1986a) noted that, because the topography slopes downward to the east, the mixed-layer depth typically becomes progressively deeper there and greater turbulent mixing is required for dryline motion to the east. (Convergence of the low-level moist air may alter this general statement.) The role of isolated topographic features is investigated here.

The purpose of the present study is to examine the creation of dryline bulges due to surface inhomogeneities under synoptically quiescent conditions using a two-dimensional version of the mixed-layer model of Jones and Bannon (2002). Following Jones and Bannon (2002), we treat the moist air east of the dryline as a mixed layer convectively driven by surface buoyancy fluxes. An elevated mixed layer that has a constant potential temperature and is decoupled from the surface lies above this moist layer. The difference between the potential temperatures of the two layers constitutes the inversion or ''lid'' that inhibits convective development. During the daytime, sensible heating is responsible for the mixing of dry air from aloft into the moist mixed layer. At night, mixing ceases and allows the inversion to reform with the aid of nocturnal radiative cooling. In addition to turbulent heat fluxes that cause convective mixing, this study adds turbulent mechanical mixing. During the day, the mechanical mixing is small compared to the convective mixing. At night the mechanical mixing is efficient in the elimination of regions in the model where the fluid depth is less than 1 m. The combination of these two mixing processes is the catalyst for dryline motion in this study. This model does not include a separate moisture flux that may be important for dryline evolution but rather treats the surface heat flux as a total buoyancy flux. Momentum mixing that is believed to contribute to bulge formation is not included in this model because Miller et al. (2001) and Jones and Bannon (2002) have shown it not to be significant in the model dynamics. Because the model only describes the dynamics of the cool moist air, the process of momentum mixing can only be incorporated to the east side of the dry front. Thus those tests by Miller et al. (2001) and Jones and Bannon (2002) of the theory of McCarthy and Koch (1982) that the movement of the dryline is associated with momentum mixing from aloft are only partial ones and are not conclusive. Anomalies of surface heat flux, inversion strength, mixed-layer depth, and topography that may affect dryline motion and contribute to bulge formation are included here. The model results examine how large-scale motions of the dryline and small-scale structures along the dryline are realized using standard mixed-layer theory (e.g., Tennekes 1973; Stull 1988).

The next section describes the physics and numerics of the mixed-layer model of the moist air mass. Section 3 presents results for a positive surface-heat-flux anomaly that affects the dryline system. Properties of the anomaly that are examined are its amplitude, orientation, and size as well as the effect of the mean synoptic geostrophic wind field. Section 4 describes the results of a negative surface-heat-flux anomaly. Section 5 describes a peak in the mixed-layer depth that propagates to the east as a nocturnal gravity wave. Section 6 presents results for topography, mixed-layer depth, and inversion strength anomalies on the dryline system.

2. The model

Figure 1 illustrates the geometry and physics of the model dryline system on an f plane. The x and y axes refer to the eastward and northward directions, respectively. The z axis is in the vertical. The u and v wind components are parallel to the x axis and y axis, respectively. The dryline model has been expanded from a one-dimensional (Jones and Bannon 2002) to a two-dimensional domain with variations in both the x and y directions.

The height of the inversion is indicated by h, the variable terrain height by η, and the fluid depth by $D = h - \eta$. Toward the eastern parts of the domain, the terrain is flat and the inversion height and fluid depth approach a value of $H_0 = 2$ km. For most model runs in this study, the terrain, η, is given by an exponential of the form

$$\eta = \eta_0 e^{-x/b}, \tag{1}$$

where $\eta_0 = 2$ km, $b = 450$ km, and $x = 0$ is the location of the dryline (where $D = 0$) at the initial time, $t = 0$. The effects of isolated hills and valleys on the dryline are examined in section 6.

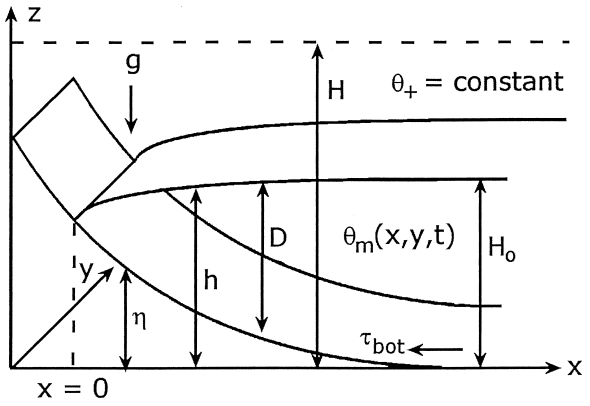

FIG. 1. Schematic diagram of the two-dimensional mixed-layer model of the dryline system on an f plane. The cool, moist mixed layer of depth D and potential temperature θ_m lies between the topography with height η and a warm, elevated mixed layer with potential temperature θ_+ An inversion of strength $\Delta\theta = \theta_+ - \theta_m$ lies at height h, and the intersection of this inversion (or dry front) with the topography denotes the dryline. The depth of the far-field inversion is indicated by H_0, which is 2 km. A southerly low-level jet exists in the cool mixed layer in addition to a background synoptic flow V_g of 8 m s^{-1}. The stress on the bottom layer is indicated by the arrow labeled τ_{bot}. Here g is gravity and H is the height (dashed line) of the reference pressure in (7).

The thermal structure of the dryline system is described by the mixed layer with a vertically uniform potential temperature, $\theta_m(x, y, t)$, that lies below an elevated mixed layer of uniform potential temperature θ_+. The elevated mixed layer is assumed to be infinitely deep with a time-independent potential temperature. The strength of the inversion is

$$\Delta\theta \equiv \theta_+ - \theta_m. \tag{2}$$

The mixed layer is in contact with the surface and undergoes a strong diurnal cycle of heating during the day and cooling at night. The daytime heating produces convective mixing that can entrain elevated mixed-layer air across the inversion and into the mixed layer. The mixed layer is also subject to time-varying mechanical entrainment that further entrains elevated mixed-layer air into the mixed layer.

There are limitations associated with the use of a mixed-layer model. In particular, its use precludes an examination of the detailed structure of the nonhydrostatic behavior of the leading edge of the dryline and the secondary internal circulations of the mixed layer. However, the results of Jones and Bannon (2002) suggest that the model has some fidelity to reality despite this limitation. Their results are in general agreement both with previous dryline simulations and with observational studies of the Great Plains springtime dryline environment. These include the eastward movement of the dryline and the steepening of the dry front during the day, the westward gradient of the mixed-layer potential temperature, the inverse effect during the night, and the development of a nocturnal low-level jet. Thus the model supports the hypothesis (Schaefer 1973, 1974a,b; Sun and Wu 1992) that boundary layer heating is sufficient to drive the dryline and explain its diurnal variation. As noted earlier in the discussion of momentum mixing, the atmosphere to the west of the model dryline is passive and has no influence on the dryline dynamics. In addition, Miller et al. (2001) noted that shallow water (and also mixed-layer) models preclude the influence of synoptic features on the dryline. Our results only apply to the synoptically quiescent case. Last, the simple 1½-layer model of the atmosphere depicted in Fig. 1 assumes an infinitely deep elevated mixed layer at rest. In reality this layer is of finite thickness is capped by a stably stratified atmosphere and contains westerly winds. As discussed later in section 3 this absence of a secondary stratification aloft will cause the model to overpredict the depth of the mixed layer in some situations. In addition the model does not allow for the advection of the model-generated plumes by the upper-level westerlies. Thus the model bulges produced here are associated with variations in surface fluxes, topography, mixed-layer depth, and inversion strength under synoptically quiescent conditions.

a. Mixed-layer equations

The continuity and momentum equations are, respectively,

$$\frac{dD}{dt} = -D\nabla\cdot\mathbf{u} + w_e, \tag{3}$$

$$\frac{d\mathbf{u}}{dt} + f\mathbf{z}\times\mathbf{u} = -\overline{\frac{1}{\rho_0}\nabla p} - \frac{\tau_{\text{bot}}}{\rho_0 D}, \tag{4}$$

where $d/dt = \partial/\partial t + \mathbf{u}\cdot\nabla$ is the horizontal material derivative, $\mathbf{u} = (u, v)$ is the horizontal velocity, $\mathbf{z}$ is a unit vector in the vertical, ∇ is the horizontal gradient operator, p is the pressure, the overbar denotes an average over the depth D, $f = 1\times10^{-4}$ s^{-1} is the constant Coriolis parameter, τ_{bot} is the stress at the bottom of the mixed layer, $\rho_0 = 1$ kg m^{-3} is a constant reference density, and w_e is the entrainment rate (Tennekes 1973) that defines the rate at which the elevated mixed-layer air is transported across the inversion into the mixed layer.

The quadratic form of surface friction (Stull 1988; Jones and Bannon 2002) is

$$\tau_{\text{bot}} = \rho_0 C_d|\mathbf{u}|\mathbf{u}, \tag{5}$$

where C_d is a dimensionless drag coefficient. Despite the dependence on surface roughness and atmospheric stability near the surface, C_d is taken to be spatially uniform. The turbulent vertical transport of momentum is being driven by both convection due to surface heating and mechanical mixing. The diurnal cycle of surface friction is applied to the dryline model in the form of a time-varying drag coefficient during the day and a constant coefficient at night, of the form

$$C_d(t) = \begin{cases} 2 \times 10^{-3}\left[1 - \cos\dfrac{\pi t}{t_{\text{ref}}}\right], & \text{for 0600 to 1800 LT} \\ 2 \times 10^{-4}, & \text{otherwise,} \end{cases} \tag{6}$$

where the constant $t_{\text{ref}} = 10$ h. This definition results in surface friction increasing from sunrise [0600 local time (LT); $t = 0$] to a maximum at 1600 LT ($t = 10$ h), and then dropping to a constant value one-tenth of the daytime drag coefficient at night. The amplitude of the drag coefficient is typical (e.g., Stull 1988) and its diurnal time dependence reflects the mechanism of Blackadar (1957) for the generation of the nocturnal low-level jet at dusk. The coefficient is initially set to zero to be consistent with the inviscid initial conditions (see section 2c) and to provide a smooth start to the numerical integration.

A depth-averaged horizontal pressure gradient (Keyser and Anthes 1977; Jones and Bannon 2002) in the momentum equation (4) has the form

$$-\overline{\frac{1}{\rho_0}\nabla p} = -\frac{g\Delta\theta}{\theta_0}\nabla h + \frac{gD}{2\theta_0}\nabla\theta_m - \frac{1}{\rho_0}\frac{\partial p'(H)}{\partial x}\mathbf{x}, \tag{7}$$

where $\theta_0 = 300$ K is a reference potential temperature in the Boussinesq approximation and $g = 10$ m s^{-2} is the acceleration due to gravity. The reference height for pressure, H (see Fig. 1), is arbitrary provided it exceeds h. Equation (7) holds rigorously for a two-layer Boussinesq fluid in hydrostatic balance. This expression takes into account the thermal structure that can exist inside and above the mixed layer. The first term on the right-hand side of (7) is analogous to the reduced-gravity term found in Miller et al. (2001). The second term is the pressure gradient force due to horizontal variations in potential temperature of the mixed layer. The third term is the synoptic-scale pressure gradient that drives motion in the mixed layer. This term is taken to be a zonal variation in pressure that drives a uniform 8 m s^{-1} geostrophic v-field V_g. This condition relieves the h and θ_m fields from having to generate the mean low-level winds. These winds are believed to participate in the evolution of the low-level jet (Blackadar 1957). Section 3 examines the impact of this synoptic-scale pressure gradient.

The thermodynamic evolution of the dryline is described (Tennekes 1973) by

$$\frac{d\theta_m}{dt} = \frac{\overline{(w'\theta')}_{\text{surface}} - \overline{(w'\theta')}_{\text{inversion}}}{D} + \dot{\theta}_{\text{rad}}, \tag{8}$$

where $\overline{(w'\theta')}_{\text{surface}}$ is the heat flux off the surface and $\overline{(w'\theta')}_{\text{inversion}}$ is the downward heat flux across the inversion that is related to the entrainment rate w_e by

$$\overline{(w'\theta')}_{\text{inversion}} = -w_e\Delta\theta. \tag{9}$$

The last term in (8) describes nocturnal radiative cooling.

The relation between the surface flux and inversion flux provide closure for the mixed-layer model. Zeman and Tennekes (1977) argue that the appropriate closure for a mixed layer overlain by an adiabatic fluid is

$$\overline{(w'\theta')}_{\text{inversion}} = -\left(\frac{C_F}{1 + C_T w_*^2\,\theta_0/gD\Delta\theta}\right)\overline{(w'\theta')}_{\text{surface}} - 2.5\frac{\theta_0 u_*^3}{gD_*}, \tag{10}$$

where the constants are $C_T = 3.55$ (Zeman and Tennekes 1977) and $C_F = 0.20$ (Tennekes 1973). Here the convective velocity scale w_* is defined by

$$w_*^3 \equiv \frac{gD}{\theta_0}\overline{(w'\theta')}_{\text{surface}}. \tag{11}$$

The second term on the right-hand side of (10) is the mechanical entrainment described by Tennekes (1973), where u_* is the friction velocity derived from (5) with the form

$$u_*^2 = \frac{|\tau_{\text{bot}}|}{\rho_0}. \tag{12}$$

To avoid excessive entrainment at small depths, we take D_* to be the maximum between D and 10 m. Mechanical entrainment is strongest within a few kilometers east of the dryline where the fluid depths are smallest. Unlike Jones and Bannon (2002), mechanical entrainment is included here for both daytime and nighttime to mix out very shallow layers on the order of a centimeter or less. In our model runs the effect of mechanical entrainment is negligible during the day, but has a large effect at night. Expression (10) is a better physical representation than the simple expression of Tennekes (1973) that uses $C_T = 0$ in (10) because it implicitly contains a horizontal dependence through D and $\Delta\theta$. Following Zeman and Tennekes (1977), bounds are placed on the entrainment rate. In particular, the entrainment rate due to convection cannot exceed 0.20 w_* while that due to mechanical entrainment cannot exceed 0.12 u_*.

The model uses a prescribed sinusoidal dependence for the diurnally varying surface heat flux. The peak is at 1230 LT (where 0600 LT is sunrise) and goes to zero just after sunset (1800 LT), at which time a constant radiative nighttime cooling rate takes effect. Therefore daytime heating is the positive portion of a sine curve that mathematically is

$$\overline{(w'\theta')}_{\text{surface}} = \begin{cases} \overline{(w'\theta')}_0 \sin\left(\dfrac{\pi t}{t_{\max}}\right), & 0600 \text{ LT} \le 1800 \text{ LT} \\ 0, & \text{otherwise,} \end{cases} \tag{13}$$

where $t_{\max}/2$ determines the time of maximum heat flux and $\overline{(w'\theta')}_0 = 0.30$ K m s^{-1}. This maximum at 1230 LT typically lags the maximum insolation (Stull 1988) and here $t_{\max}$ is taken as 13 h. The cessation of the flux

at dusk is consistent with the time dependence of the drag coefficient (8) that describes the Blackadar (1957) mechanism of a sharp reduction of the fluxes at dusk. The value of radiative cooling, $\dot{\theta}_{\text{rad}} = -0.330$ K h^{-1}, is approximately that needed to restore the inversion strength overnight. By defining the surface heat flux by (13), the inversion heat flux is diagnosed using (10) and the entrainment is found using (9).

b. Model numerics

The governing equations are solved using finite differencing with the conservative flux form as described by Jones and Bannon (2002). The grid resolution is 5.0 km on a model domain of 1700 km in x and 1700 km in y. The domain size models that of the U.S. Great Plains. The x direction roughly spans the region from central New Mexico to the Mississippi River, and the y direction spans that from south-central Texas to the Nebraska–South Dakota border. The use of such a large domain minimizes the effects of the open boundaries. The time step is 20 s.

c. Initial and boundary conditions

The initial conditions of the model are an exact, nonlinear, uniform potential vorticity, steady-state solution without friction ($\tau_{\text{bot}} = 0$) and without entrainment ($w_e = 0$) for the exponential topography (1). The initial conditions for h and v (see Fig. 2 of Jones and Bannon 2002) exhibit a low-level jet with a maximum of 23 m s^{-1} at the western edge of the dryline system where $D = 0$. There is no initial u velocity. The maximum depth of the mixed layer is 2 km in the far field. These conditions are valid at 0600 LT ($t = 0$) for the dryline system. The v field decays exponentially with distance from the dryline and approaches $V_g = 8$ m s^{-1} in the far field.

The northern ($y = 1200$ km), southern ($y = -500$ km), and eastern ($x = 1100$ km) boundaries are open such that the normal gradient of each variable is set to zero. This condition is acceptable because tests showed that there is little reflection at the eastern and meridional boundaries and they are far removed from the anomalies. The western edge of the fluid where D and θ_m vanish is treated following Schär and Smith (1993) and Schär and Smolarkiewicz (1996). This scheme uses an upstream differencing of the advective terms in flux form that keeps the fluid depth D and mixed-layer temperature θ_m nonnegative with a flux correction to reverse the effects of the computational diffusion. Momentum averaging, rather than velocity averaging, is used to keep the velocity fields bounded in regions where fluid depth is vanishing.. Tests of the algorithm (Schär and Smith 1993; Schär and Smolarkiewicz 1996; Miller et al. 2001) indicate that the scheme can accurately handle both advancing and retreating layers of fluid.

d. Perturbations

The structure of the anomalies in the topography η, surface heat flux $\overline{(w'\theta')}_{\text{surface}}$, mixed-layer depth D, and mixed-layer potential temperature θ_m, is given by a normalized Gaussian distribution of the form

$$G' = A \exp\left[-\frac{(x' \cos\alpha + y' \sin\alpha)^2}{2\sigma_x^2} - \frac{(-x' \sin\alpha + y' \cos\alpha)^2}{2\sigma_y^2}\right], \quad (14)$$

where G' is the Gaussian anomaly of the field added to the preexisting field; A is the normalized amplitude of the anomaly with form $A = A_0\sigma_0^2/\sigma_x\,\sigma_y$, where A_0 and σ_0 (=500 km) are nonnormalized amplitude and dimension values that define the anomaly; σ_x and σ_y denote the zonal and meridional spatial dimensions; and $x' = x - x_0$ and $y' = y - y_0$ denote the zonal and meridional distance from the center of the anomaly at (x_0, y_0). Normalizing the Gaussian provides the ability to alter the spatial size of the anomaly without changing its area integral. Typically, the anomaly center is 200 km east of the initial dryline position and 500 km north of the southern boundary. Rotation of the anomaly is possible through the angle α. Anomalies of topography simulate peaks and valleys as they are added to the exponential topography and are time independent. Surface heat flux anomalies simulate hot or cold areas within the domain with respect to a background surface heat flux of 0.30 K m s^{-1}. These heat fluxes vary in time with the diurnal heating cycle (13), but are spatially fixed within the domain. Initial anomalies of mixed-layer depth simulate a change in mass within the column, and these anomalies will change in time and space as the dry front evolves during the model run. Similarly initial mixed-layer potential temperature anomalies simulate changes in the inversion strength with respect to a background value of 6 K through (2) and will also evolve with time during the model run.

3. Positive surface-heat-flux anomalies

In order to determine the effects of different anomalies on the dryline system, we first present a benchmark case in section 3a. This benchmark case is a circular, positive surface-heat-flux anomaly. Section 3b describes the effect of rotating an elliptical surface-heat-flux anomaly. Section 3c examines the effect on the dryline motion when the amplitude of the anomaly is varied compared to the benchmark case. Section 3d describes the effect of varying the size of the anomaly. Section 3e considers the effect of changing the background synoptic geostrophic wind V_g with a benchmark heat flux anomaly. All sections present daytime dryline motion, but nighttime motion is considered only for the benchmark.

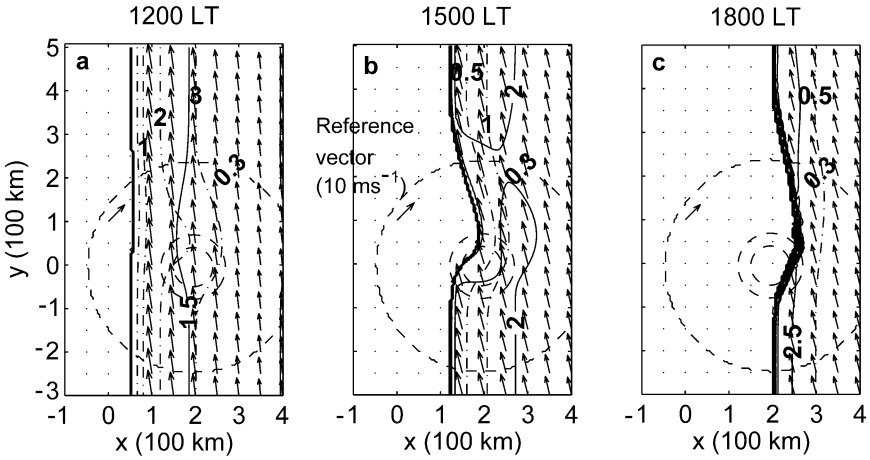

FIG. 2. Contour plots of the benchmark case in x–y space for (a) 1200, (b) 1500, and (c) 1800 LT. Contours of the mixed-layer depth D are indicated by solid lines with a contour interval of 0.5 km and contour labeling rotated 90°. Wind direction (u, v) and speed in the mixed layer are indicated by arrows plotted at 50-km intervals. A reference vector of 10 m s^{-1} is indicated in each panel. Inversion strength is indicated by dashed–dotted lines with a contour interval of 1 K plus a 0.5-K contour closest to the dryline location. The inversion strength contour labeling is vertical. Surface heat flux anomaly contours are given by dashed lines with a contour interval of 0.05 K m s^{-1}, with the labeling rotated 45°. The background surface heat flux is 0.30 K m s^{-1}, with an anomaly amplitude of 0.15 K m s^{-1}. This plot and other non-high-resolution contour plots are portions of the entire domain. Contour intervals in this figure are used in subsequent contour figures only. All labeling conventions and important contours labeled with bold face numbers are used in subsequent figures.

In all experiments the initial model time $t = 0$ corresponds to 0600 LT. The benchmark case and all other model runs presented in this paper include mechanical mixing and friction as described previously. All model runs use exponentially decaying topography as described by (1) except for the topography anomalies of section 6. All runs use the initial conditions of Fig. 2 of Jones and Bannon (2002) except for the initial condition anomaly runs of section 6.

The dryline movement is measured using the zero fluid depth contour ($D = 0$). For all cases the length and width of the daytime dryline bulge at 1800 LT is determined. The length is measured from data output from the first point of bulging to the last point along the meridional direction. The width is measured from the unperturbed section of the dryline to the depth contour farthest to the east within the bulge. The maximum peak depth at 1800 LT is determined by creating high-resolution plots around the dryline bulge and noting this peak in kilometers. Finally, the speed of the gravity wave that propagates to the east at night is found by noting its position every 3 h and determining the mean for each 3-h period.

a. Benchmark case

The benchmark case consists of an initial background surface heat flux of 0.30 K m s^{-1} and a circular heat flux anomaly whose center amplitude is $A_0 = 0.15$ K m s^{-1} for a total of 0.45 K m s^{-1}. The spatial size of the anomaly is $\sigma_x = \sigma_0 = 500$ km by $\sigma_y = \sigma_0 = 500$ km, and the synoptic v field V_g is 8 m s^{-1}. The initial parameter settings are a spatially uniform inversion strength $\Delta\theta$ of 6 K and a far-field depth H_0 of 2 km.

The placement of the anomaly center requires some explanation. In the x direction, if the anomaly center is placed too close to the initial dryline position at $x = 0$, the effect of the anomaly is minimal because the dryline quickly moves to the east during the day. When the anomaly is placed in the far field where mixed-layer depth is 2 km, there is insufficient time for the anomaly to produce a bulge. The location of the anomaly center in the y direction is chosen in order to avoid boundary effects along the southern boundary ($y = -500$ km) and prevent waves along the dryline from propagating to the northern boundary ($y = 1200$ km).

Figure 2 shows the evolution of the dryline system during the day. Initially at 0600 LT (not shown) the dryline is located at $x = 0$ km with no variation in the y direction. At 1200 LT (Fig. 2a), the dryline is moving eastward as daytime heating mixes out the shallowest parts of the moist layer. The effect of the anomaly is beginning to become apparent: there is an enhanced region of motion downstream from the anomaly along the dryline. The effect on dryline motion is not centered at the region of greatest heating due to advection by the mean flow. Near the anomaly, $\Delta\theta$ is decreased and the inversion-strength contours bulge eastward. In contrast the depth of the mixed layer is increased and the 1.5-km depth contour bulges westward.

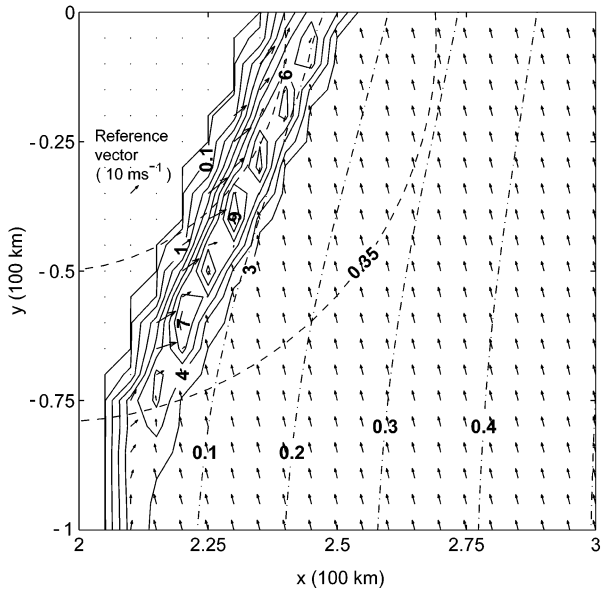

FIG. 3. High-resolution contour plot of Fig. 2c along the dryline bulge in *x*–*y* space at 1800 LT. Depth contour interval is 1 km. The two leftmost solid lines are 1- and 100-m-depth contours, which appear in subsequent figures. Surface heat flux anomaly contour interval remains at 0.05 K m s^{-1}. Inversion strength contour interval is 0.1 K. Wind vectors are plotted at each grid point. Contour intervals (except wind vectors) in this figure are used in subsequent high-resolution figures.

At 1500 LT (Fig. 2b) the dryline is nearing the center of the anomaly and an eastward bulge in the dryline appears. As the dryline bulge becomes more pronounced, the angle between the southern edge of the bulge and the winds become more perpendicular, thereby increasing convergence along the dryline. This convergence in turn leads to a tightening of depth contours that indicates the dryline is becoming more vertical.

By 1800 LT (Fig. 2c), the dryline has passed the area of maximum heat flux. By this time the heat flux (13) has vanished. Due to this decrease in heating, the dryline bulge width is smaller than 3 h earlier. The section of the dryline not affected by the heat flux anomaly has moved 200 km east, but the bulge has moved an additional 60 km due to enhanced convective mixing. Figure 2c shows that the angle between the bulge and the winds are less perpendicular than 3 h ago, so one might expect less convergence. However, mixed-layer depths reach several kilometers as the dryline becomes vertical.

Figure 3 presents more information on the fine structure along the dryline bulge at 1800 LT in a 100 km × 100 km region where the greatest mixed-layer depths are found. Southeasterly winds at 12 m s^{-1} combined with southwesterly winds at 25 m s^{-1} contribute to sufficient convergence along the dryline to produce mixed-layer depths of up to 9 km. Downstream of the anomaly the convergence is weaker and the mixed-layer depth reaches up to 6 km. The inversion strength in the far field decreases to 1 K, but peaks greater than 6 km along the dryline fall within a region of very weak inversion strength (less than 0.1 K). The weaker inversion strength near the dryline than in the interior to the east is a consequence of the larger warming produced where the mean mixed-layer depth is shallower (see Fig. 1).

It is important to note that the grid resolution is 5 km in both *x* and *y*. The fine structure displayed in Fig. 3 is thus not numerical noise. Higher-resolution runs (not shown) also display similar fine structure that is slightly narrower in width with larger peaks.

The weak inversion strengths and large mixed-layer depths are pushing the limits of the mixed-layer model. We interpret these features as the loci for the onset of deep moist convection, a process that lies beyond the model physics. In reality the moist air is overlain by an elevated mixed layer (e.g., Schaefer 1986a) that extends through the midtroposphere to about 5 km above which the air is stably stratified. Inclusion of this stable layer is precluded in the present 1½-layer model configura-

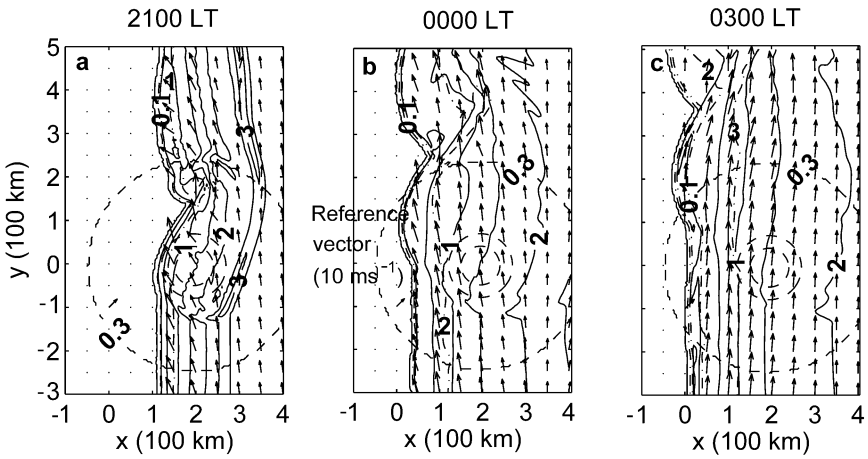

FIG. 4. Contour plots of the benchmark case in *x*–*y* space for (a) 2100, (b) 0000, and (c) 0300 LT. Surface heating has terminated, but the heat flux anomaly contours are still plotted for reference.

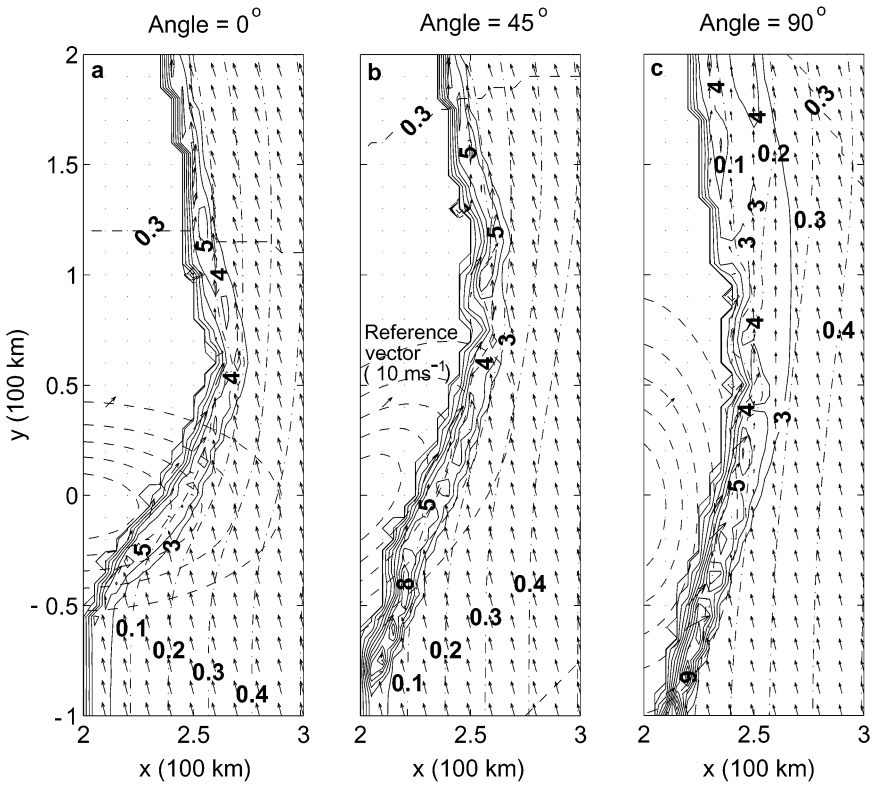

FIG. 5. High-resolution contour plots along the dryline bulge in x–y space at 1800 LT for (a) 0°, (b) 45°, and (c) 90° rotation of a positive, elliptical, surface heat flux anomaly. Maximum surface heat flux amplitude is 0.60 K m s^{-1}, at the anomaly center. Wind vectors are plotted every 10 km for this and subsequent high-resolution plots unless stated otherwise.

TABLE 1. Dryline bulge characteristics for all positive and negative surface heat flux anomaly cases at 1800 LT. The benchmark case has a circular anomaly of 0.15 K m s^{-1} amplitude, 500 km × 500 km size, and a synoptic geostrophic wind V_g of 8 m s^{-1}.

Model run	Bulge width (km)	Bulge length (km)	Peak depth max (km)
Benchmark	60	475	9
Rotation			
0°	75	450	5
45°	60	475	8
90°	50	600	9
Amplitude			
0.075 K m s^{-1}	40	400	6
0.30 K m s^{-1}	80	575	8
0.60 K m s^{-1}	120	675	7
Size			
125 km^2	20	275	6
250 km^2	40	325	7
1000 km^2	115	750	7
Pressure gradient			
5 m s^{-1}	65	450	8
10 m s^{-1}	50	575	9
15 m s^{-1}	50	650	10
Negative heat flux	75	450	8

tion. Thus the model tends to overpredict the amplitude of the peaks. Unsaturated boundary layer plumes in nature would not penetrate far into this stable layer. Saturated conditions would lead to deep convection that extends to the tropopause and is often observed in the vicinity of the dryline (e.g., Rhea 1966).

Figure 4 documents the nocturnal structure of the dryline. After 1800 LT, the surface heating has ceased and radiative cooling has commenced abruptly. The westward surge of the dryline at 2100 LT (Fig. 4a) follows a dam-break effect (Miller et al. 2001) that begins when heating ceases. Three hours later at 0000 LT (Fig. 4b), the dryline continues a westward surge as the winds still have an easterly component. It is also at this time that the low-level jet reaches a maximum of 21 m s^{-1} near the dryline. The addition of mechanical mixing prevents the westward surge of very shallow fluid depth ($D < 1$ m) from traveling beyond $x = 0$ km in the zonal direction. In previous runs (not shown) without nocturnal mechanical mixing, the dryline surged to $x = -200$ km but with fluid of very shallow depths (<1 m) to the west of $x = 0$. Figure 4c shows that by 0300 LT the Coriolis force has deflected the westward flow to the north, or even north-

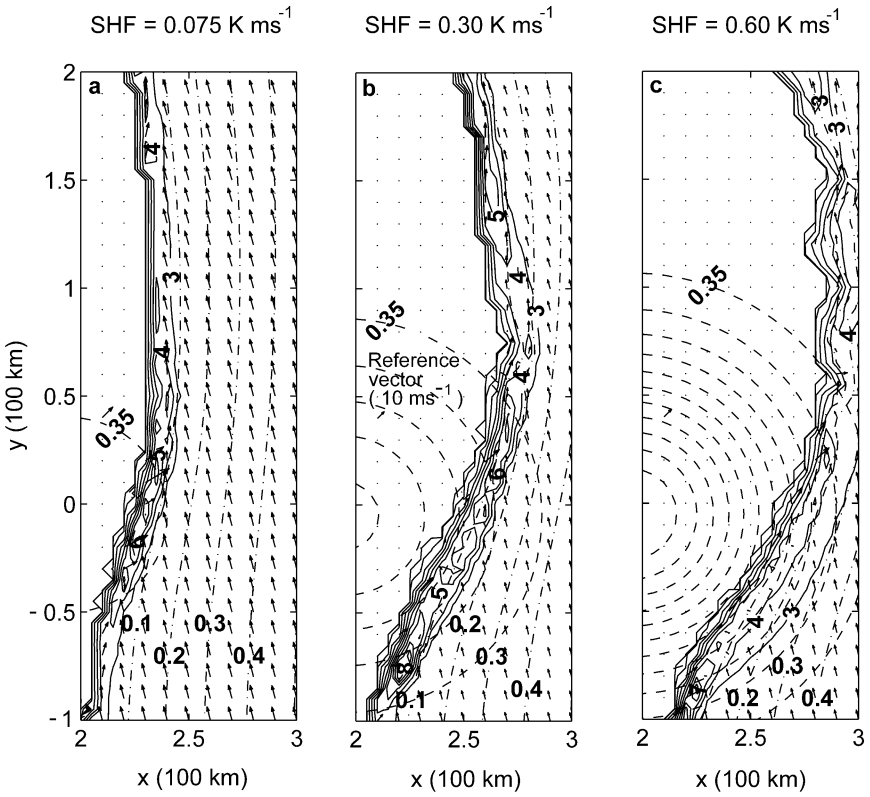

FIG. 6. High-resolution contour plots along the dryline bulge in *x*–*y* space at 1800 LT for a positive, circular surface heat flux anomaly with maximum amplitude SHF of (a) 0.075, (b) 0.30, and (c) 0.60 K m s^{-1}.

east, thereby halting the westward surge. In addition to the turning of the winds, the constant radiative cooling rate of -0.330 K h^{-1}, which cools the moist mixed-layer air and makes it more dense, forces air eastward down the topography by gravity and thus helps to halt the surge. This cooling also acts to restore the inversion strength to 5 K in the far field. Although not shown, from 0300 to 0600 LT the dryline does not move back eastward. This behavior is attributed to the presence of the nocturnal friction near the dryline that varies inversely with the fluid depth [see (4)] and thus significantly affects the shallow fluid of depth less than 100 m at 0000 LT and decreases the wind speed compared to the deeper fluid. As a result, the Coriolis force is weaker and winds tend not to turn westerly for the shallow fluid. However, at fluid depths greater than 100 m, the depth contours do move toward the east because the winds are strong enough for the Coriolis force to dominate.

b. Orientation effects

Three model runs are performed to determine the effect of rotating an elliptical heat flux anomaly on the dryline. The elliptical anomaly is defined by $A_0 = 0.15$ K m s^{-1}, $\sigma_x = \sigma_0 = 500$ km, and $\sigma_y = 250$ km. Its maximum amplitude is 0.30 K m s^{-1} due to the normalization of the Gaussian. The overall amplitude, including that of the background is now 0.60 K m s^{-1}. The area integral of each elliptical anomaly is the same and is identical to that for the circular benchmark case. The orientation of the anomaly is varied by varying the angle α. All other parameters are the same as the benchmark case.

Figure 5 depicts the structure of the dry front system at 1800 LT for the elliptical anomaly rotated 0°, 45°, and 90°. Table 1 summarizes the attributes of the dryline bulge and peaks in the mixed-layer depths for these cases. Table 1 indicates that the bulge length increases from 450 km for the 0° case to 600 km for the 90° case. This increase is expected because a meridionally larger anomaly will affect a larger portion of the dryline. In contrast, the width of the bulge decreases as the angle is increased. This decrease arises because the dryline passes over a zonally narrower anomaly faster than a wider one. For example, a large portion of the nonrotated anomaly lies to the east of the dryline by 1800 LT but the 90° dryline has passed over most of the anomaly. Last, as the anomaly angle increases toward 90°, the anomalies are more efficient at generating larger peaks in the depth of the mixed layer.

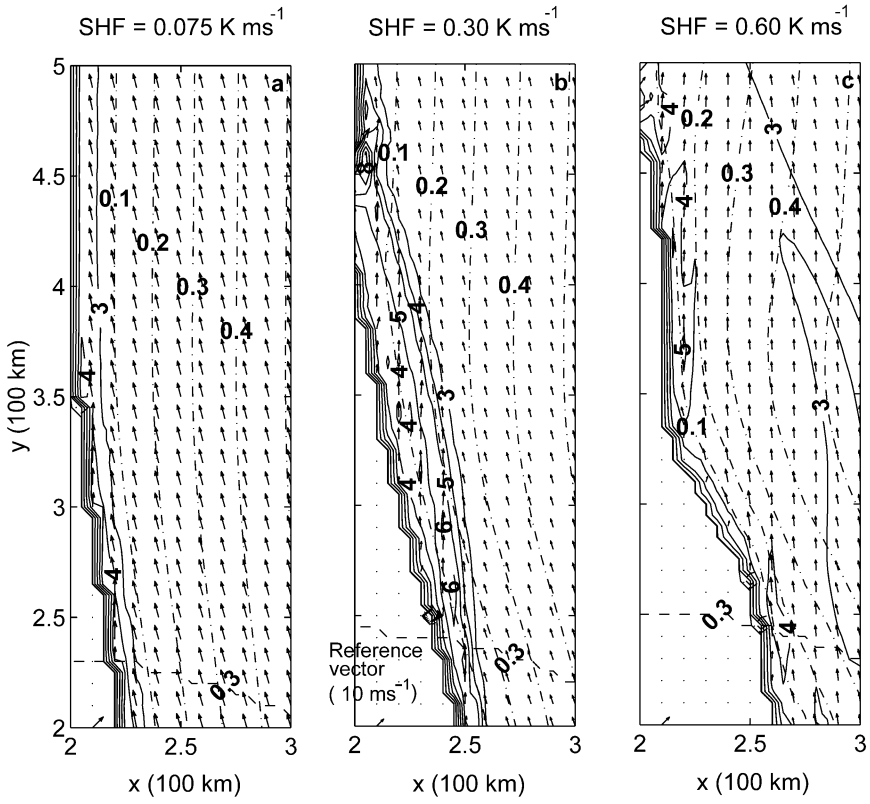

FIG. 7. As in Fig. 6 except farther downstream of the anomaly center.

c. Amplitude effects

Figure 6 and Table 1 compare the effect of circular heat flux anomalies with the same size as that of the benchmark but with amplitudes one-half, two times, and four times that of the benchmark. Specifically anomalies of $A_0 = 0.075$ K m s^{-1} (Fig. 6a), 0.30 K m s^{-1} (Fig. 6b), and 0.60 K m s^{-1} (Fig. 6c) are added to the background heat flux. Note that the areas of the anomalies are equal. All other parameters are the same as the benchmark case otherwise.

Table 1 summarizes the results for these cases and shows that, as the amplitude of the heat flux anomaly increases from 0.075 to 0.60 K m s^{-1}, the bulge width and the bulge length increase as expected. One might also expect there to be greater mixed-layer peaks in Fig. 6c because the dryline has passed through the greatest heating. The absence of larger peaks may be due to the fact that the increased heating mixes out the air too quickly. Farther downstream of the anomaly center in Figs. 7b and 7c there is evidence of local minima in the mixed-layer depth similar to Fig. 5c. As the heat flux increases, the region near the dryline becomes wider and these minima start to occur. Currently there is no explanation for why the dryline spreads like this.

A comparison between the rotated anomalies and the circular anomaly with amplitude 0.30 K m s^{-1} (Fig. 6b) can be made with the expected results. The spatial size of the anomalies in Figs. 5a and 6b are $\sigma_x = 500$ km. Table 1 compares the bulge width for these two cases and shows a width of 75 km for the 0° rotated anomaly and a width of 80 km for the circular anomaly. The spatial size of the anomalies in Figs. 5c and 6b are $\sigma_y = 500$ km. Table 1 compares the bulge length and reveals a length of 600 km for the 90° rotated anomaly and a length of 575 km for the circular anomaly. These comparisons indicate that circular and elliptical anomalies with equal amplitude and spatial dimension can produce very similar bulge characteristics. The regions near the dryline in Figs. 5b and 6b have the greatest resemblance in appearance. Despite having equal heat flux amplitude, the bulge width of 80 km in Fig. 6b is greater than the bulge width of 60 km in Fig. 5b because the heat flux width in Fig. 6b is larger. The bulge length in Fig. 6b is 575 km versus a bulge length of 475 km in Fig. 5b. Once again the heating amplitude is the same but the heating anomaly has greater length in Fig. 6b than in Fig. 5b, suggesting that the bulge length is proportional to the anomaly length.

d. Size effects

A comparison of heat flux anomalies with different spatial size is performed to determine the effect on the dryline bulge. Dimensions of the anomaly are changed

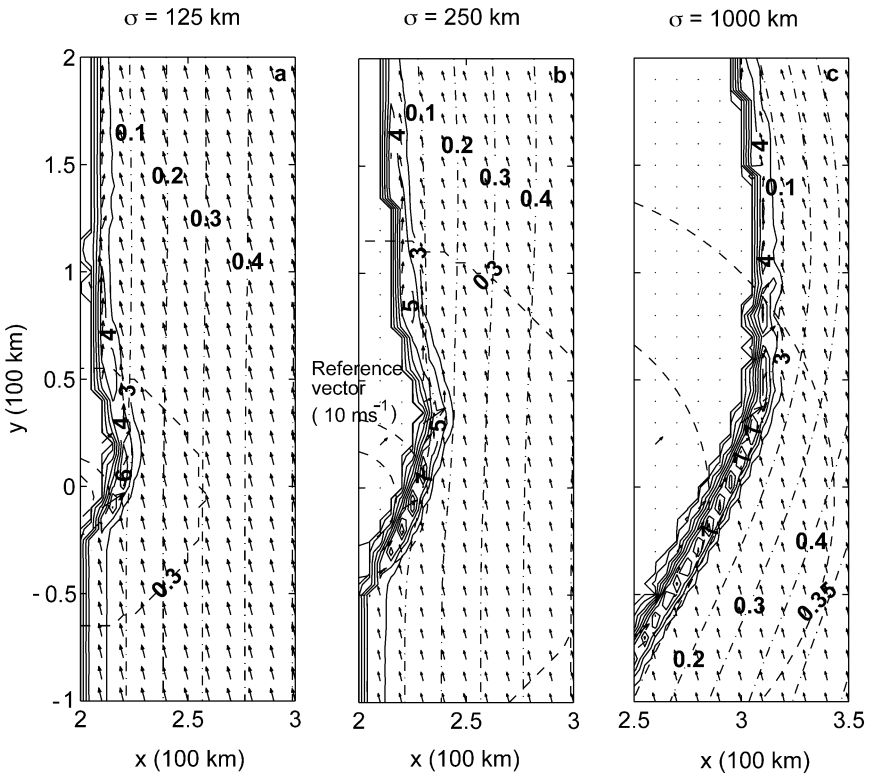

FIG. 8. High-resolution contour plots along the dryline bulge in *x–y* space at 1800 LT for a positive, circular surface heat flux anomaly with dimension σ of (a) 125, (b) 250, and (c) 1000 km.

so that $\sigma = \sigma_x = \sigma_y = 125$ km (Fig. 8a), $\sigma_x = \sigma_y = 250$ km (Fig. 8b), and $\sigma_x = \sigma_y = 1000$ km (Fig. 8c). These cases are compared to the benchmark case of $\sigma_x = \sigma_y = 500$ km and all other parameters are the same as the benchmark case. The Gaussian normalization ensures that, as the anomaly size increases, the area integral of the anomaly remains constant. Table 1 shows that as the *x* and *y* dimensions are doubled, the bulge width increases linearly to 40 km, but then nearly doubles in size to 115 km in the 1000 km case. The dryline bulge also increases as the size of the anomaly increases in nonlinear fashion.

e. Synoptic pressure gradient effects

The effect of the background synoptic pressure gradient is studied by altering the meridional geostrophic wind speed V_g from its value of 8 m s^{-1} for the benchmark. The amplitude and size of the heat flux anomaly is the same as the benchmark case with every other parameter being the same as well. As the wind speed is increased from 5 (Fig. 9a) to 15 m s^{-1} (Fig. 9c), the portion of the dryline not affected by the enhanced heating moves 35 km less toward the east. In addition, as Table 1 indicates, the dryline bulge also decreases as the pressure gradient increases. Both of these trends are explained by a stronger easterly component of the wind that inhibits eastward motion of the dryline. This easterly component is the result of friction producing a cross-isobaric flow toward the west. The bulge length increases (see Table 1) as the synoptic winds increase due to greater advection along the dryline. Mixed-layer peaks increase from 8 km at $V_g = 5$ to 10 km at 15 m s^{-1} because of the greater convergence that can be seen in Fig. 9 by merging wind vectors. Similar to the increased heat flux anomaly amplitude, the case in Fig. 9c begins to show a local minimum in mixed-layer depth at $y = 175$ km.

4. Negative surface-heat-flux anomaly

A model run with a negative heat flux anomaly is performed for a comparison to the positive anomaly of the benchmark. All parameters are the same as in the benchmark case except that the anomaly is negative and has total amplitude of 0.15 K m s^{-1} at the center of the anomaly. At 1200 LT (Fig. 10a) there is very little effect of the negative anomaly on the dryline. The 1.5-km depth contour bulges to the east indicating less convective mixing and hence a decrease in the entrainment of elevated mixed-layer air into the moist air. The reduced heating also helps to preserve a higher inversion strength. The background surface heat flux of 0.30 K m s^{-1} still provides sufficient mixing away from the

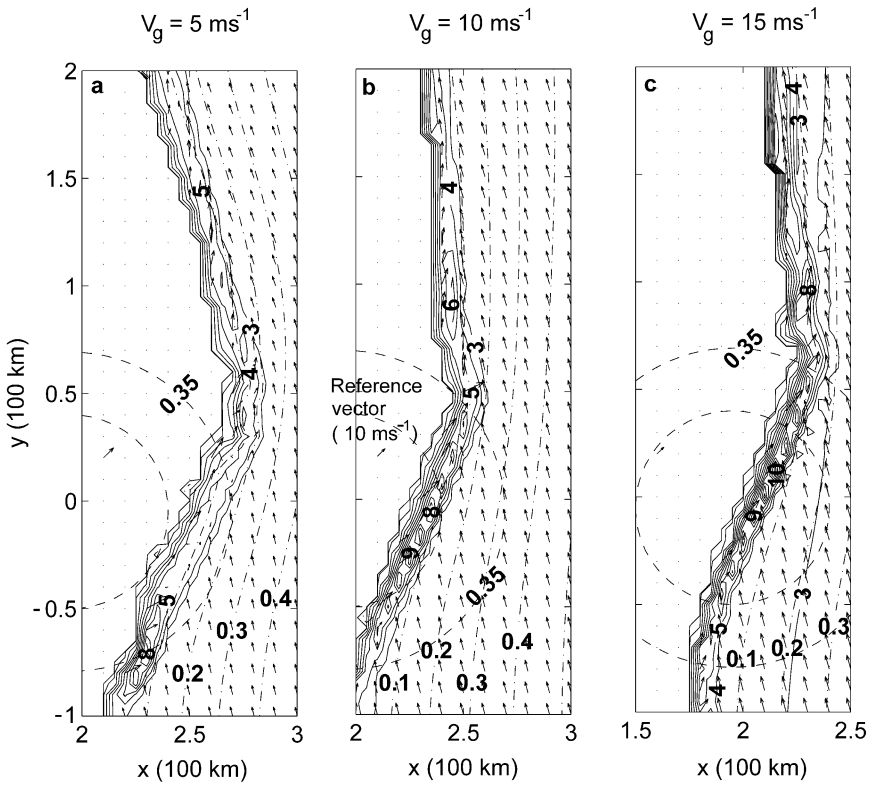

FIG. 9. High-resolution contour plots along the dryline bulge in *x–y* space at 1800 LT for a surface heat flux anomaly defined in the benchmark case and background synoptic geostrophic wind V_g of (a) 5, (b) 10, and (c) 15 m s^{-1}.

anomaly to move the dryline eastward. As in the positive anomaly case, the effect of the anomaly appears downstream due to advection. Three hours later at 1500 LT (Fig. 10b), the dryline nears the heating minimum that inhibits mixing and a dryline bulge toward the west appears.

By 1800 LT (Fig. 10c), the dryline has passed the area of minimum heating and a large portion of heating remains on the moist side of the dryline. Unlike the benchmark case where the greatest bulge width occurs at 1500 LT, here the bulge width is a maximum at 1800 LT. This behavior occurs because there is still half of the negative anomaly that the dryline has yet to pass. The section of the dryline not affected by the anomaly

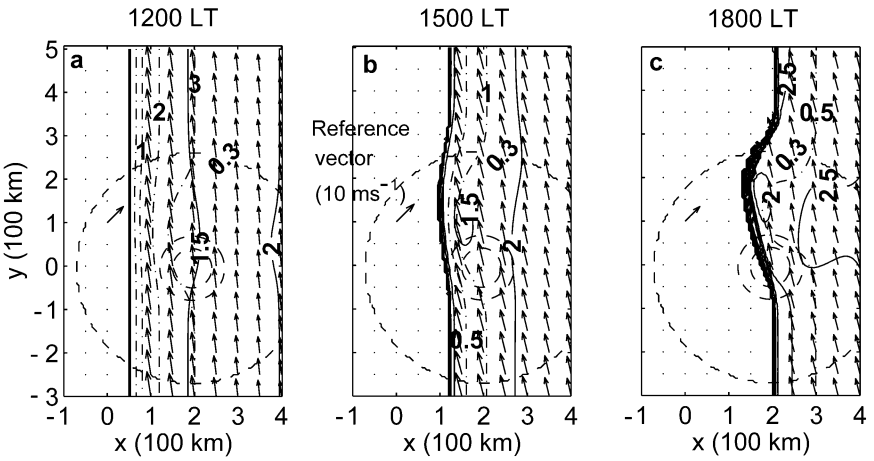

FIG. 10. Contour plots of a negative, circular heat flux anomaly in *x–y* space for (a) 1200, (b) 1500, and (c) 1800 LT. The anomaly amplitude is −0.15 K m s^{-1} added to a background of 0.30 K m s^{-1}. All other parameters as in Fig. 2.

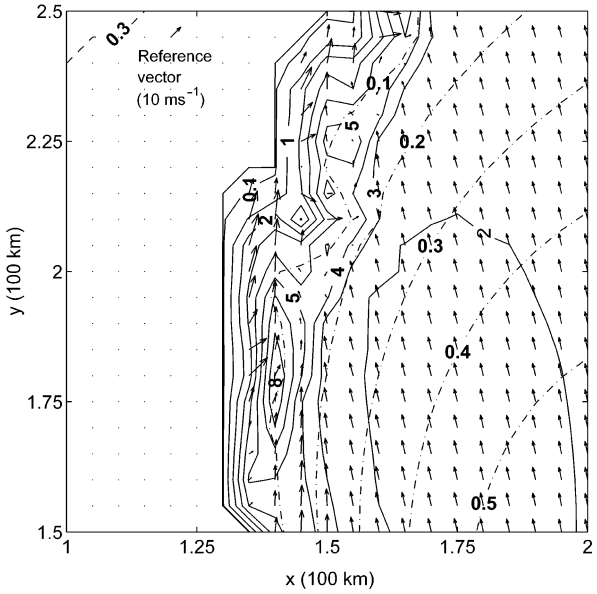

FIG. 11. High-resolution contour plot of Fig. 10c along the dryline bulge in *x*–*y* space at 1800 LT. Wind vectors are plotted every grid point.

moves 200 km eastward as in the benchmark case, but the bulge has lagged 75 km behind the dryline. Figure 10c shows that the angle between the bulge and the winds are most perpendicular along the northern edge of the bulge, which supports the greatest convergence. As in the benchmark case, the dryline becomes vertical by this time, as evidenced by the tight depth contours. Table 1 shows that the negative anomaly has a bulge length 25 km shorter, but the bulge width is 15 km wider than that of the positive anomaly. The latter feature is more significant because it is a greater fractional change.

Figure 11 presents a 100 km by 100 km plot of the bulge where the greatest mixed-layer depths are found. Southeasterly winds at 10 m s^{-1} combined with southwesterly winds at 20 m s^{-1} contribute to the strong convergence along the dryline. Note, however, that only one very high peak of 8 km forms with a negative heat flux anomaly compared to many peaks greater than 6 km in the benchmark case.

After 1800 LT, surface heating ceases and the dryline retrogresses westward (Fig. 12). Much of the westward surge characteristics and physical explanation is the same for the negative anomaly as it is for the benchmark case. The one difference at night is that the surge downstream of the heat flux minimum is farther west only because this part of the dryline lagged behind during the day.

5. Nocturnal mixed-layer gravity wave

As the model dryline surges westward at night, a broad region of enhanced mixed-layer depth forms and moves eastward. This wave feature is seen in Fig. 4a at $x = 300$ km and $y = 300$ km. A westerly wind component is associated with the wave. The wave is very narrow with a width of 20 km in the zonal direction, but it can be several hundred kilometers long in the meridional direction. A 3-h-averaged phase speed is determined for the wave and is shown in Table 2 for the benchmark, negative heat flux, and synoptic-pressure-gradient model runs. The wave depth at 1900 LT increases as the synoptic pressure gradient increases because of the stronger southeasterly winds that contribute to greater convergence. For all runs, the wave depth decreases by 0000 LT (not shown) to the depths shown for 0600 LT. As the wind increases due to the synoptic pressure gradient, the length of the wave grows in the meridional direction and is advected farther downstream over time from its initial position at 1900 LT.

Phase speeds are determined over 3-h averages. From 2100 to 0000 LT the speed of the wave is generally

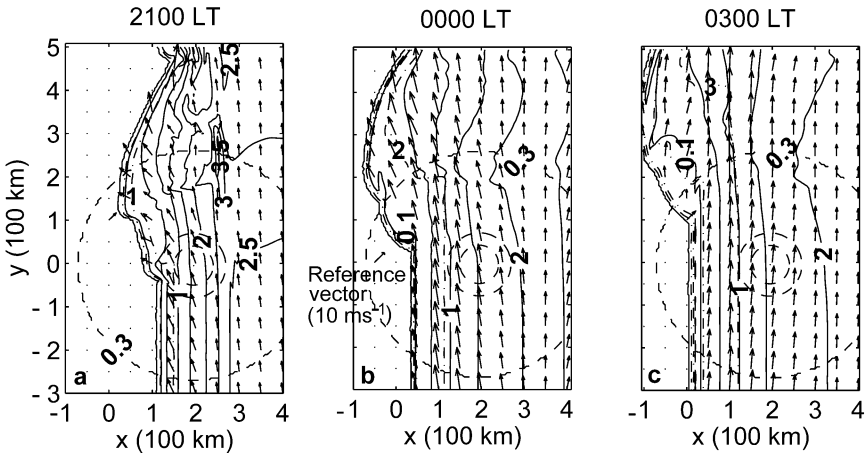

FIG. 12. Contour plots of a negative, circular heat flux anomaly in *x*–*y* space for (a) 2100, (b) 0000, and (c) 0300 LT. Surface heating has terminated by 1800 LT, but the heat flux anomaly contours are plotted for reference.

TABLE 2. Averaged zonal speed (m s^{-1}) of the mixed-layer gravity wave over three 3-h intervals at night. The wave depth is that above the reference far-field depth H_0 of 2 km.

Model run	2100–0000 LT	0000–0300 LT	0300–0600 LT	Wave depth at 1900 LT (km)	Wave depth at 0600 LT (km)
Benchmark	15	18.5	21.5	2.5	0.5
Pressure gradient					
5 m s^{-1}	15.25	18.75	21.75	2.0	0.5
10 m s^{-1}	15.5	19.25	22.25	2.5	1.0
15 m s^{-1}	17.0	20.5	23.25	3.5	1.5
Negative heat flux	15.25	18.5	21.25	1.0	0.25

15 to 17 m s^{-1}, and the westerly wind component is 5 m s^{-1}. Over the next 3-h period the average phase speed increases to 18.5 to 20.5 m s^{-1}, and the westerly wind component is still 5 m s^{-1}. Radiative cooling is strengthening the inversion and, because the phase speed is proportional to the square root of the inversion strength, the wave travels faster as the night progresses. The trend in wave speed during this second 3-h period increases with increasing synoptic pressure gradient nonlinearly as seen in Table 2. For the final 3-h period from 0300 to 0600 LT, the phase speed has increased to 21.5 to 23.25 m s^{-1}, which is a smaller increase than the prior time period because the inversion strength increase has slowed. The westerly wind component has decreased slightly to 4 m s^{-1}.

6. Effects of topography and initial conditions

Three other types of anomalies are added to the model to study the dryline motion. The first anomaly is that due to topography. Topography can have an influence on the dryline, so a peak (Fig. 13a) and a valley (Fig. 14a) are added to the background exponentially decaying topography (1) representing the Great Plains. The peak can be regarded as a single mountain (e.g., a mountain in the Ozarks) or a plateau region in west-central Texas. These features are reasonably well represented by a constant Gaussian peak added to the model with an amplitude $A = 500$ m, and a spatial size $\sigma_x = \sigma_y = 200$ km. All model parameters and processes are the same as the benchmark case except that there is a uniform surface heat flux over the domain. Figure 13a shows dotted lines, which represent 250-m contours in topography, and the positive anomaly is centered at the same place as the surface heat flux anomaly from the benchmark case. Initially a peak creates a shallower mixed layer that is advected downstream of the anomaly center and creates a bulge toward the east by 1800 LT (Fig. 13a). With a shallower mixed layer, the uniform heating can act more quickly to entrain warm air into the layer. Mixed-layer peaks up to 6.5 km (not shown) are formed along the edge of the bulge most perpendicular to the winds due to convergence. For a negative topography anomaly (Fig. 14a), an initially deeper

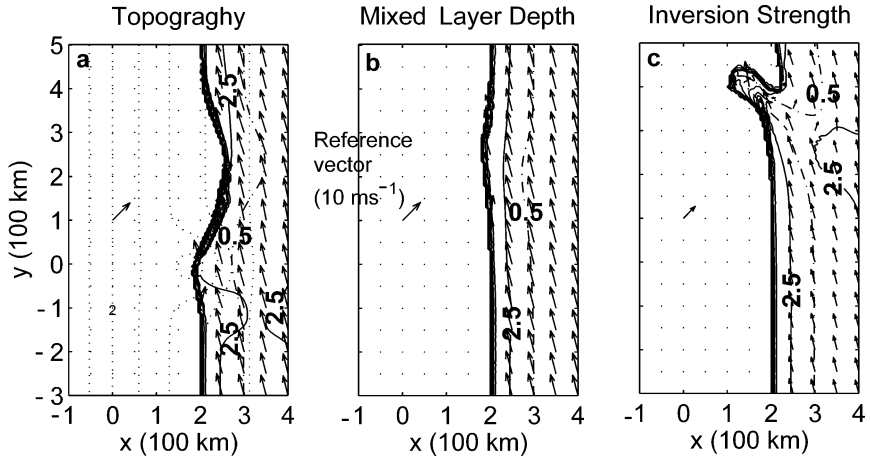

FIG. 13. Contour plots for positive, circular anomalies in x–y space at 1800 LT. (a) A topography peak of 500 m above the surrounding area with dotted lines indicating contours with an interval of 0.25 km decreasing exponentially toward the right. The 2-km contour is located at $x = 0$ km of the domain. (b) An initial condition where the mixed-layer depth anomaly is 0.5 km higher than the background at that location and changes over time. (c) An initial condition where the inversion strength anomaly is 2 K higher than the background value of 6 K and changes over time. These anomalies are initially centered at the same place as that in Fig. 2.

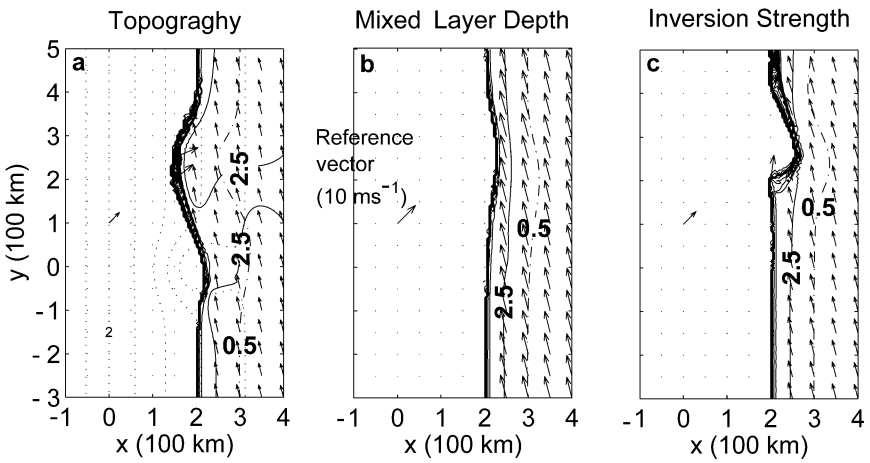

FIG. 14. Contour plots for negative, circular anomalies in x–y space at 1800 LT. (a) A topography valley of 500 m below the surrounding area with dotted lines indicating contours with an interval of 0.25 km decreasing exponentially toward the right. The 2-km contour is located at $x = 0$ km of the domain. (b) An initial condition where the mixed-layer depth anomaly is 0.5 km lower than the background at that location and changes over time. (c) An initial condition where the inversion strength anomaly is 2 K lower than the background value of 6 K and changes over time. These anomalies are initially centered at the same place as that in Fig. 2.

mixed layer is advected downstream. Because a deeper mixed layer takes longer to be mixed out, a dryline bulge is created toward the west. The bulge at 1800 LT contains mixed-layer peaks up to 10 km in the region (Fig. 14a) where wind vectors are pointing almost due east.

The second anomaly is a variation in the initial mixed-layer depth with an amplitude $A = 500$ m and a spatial size $\sigma_x = \sigma_y = 200$ km. Its initial location is $(x_0, y_0) = (200 \text{ km}, 0 \text{ km})$. Again, all model parameters and processes are the same as the benchmark case except that there is a uniform surface heat flux over the domain. Because the mixed-layer anomaly is a characteristic of the air, the anomaly changes over time and is advected downstream. Positive and negative anomalies are contrasted in Figs. 13b and 14b. By 1800 LT (Fig. 13b) the amplitude of the anomaly has decreased and the dryline bulge it creates is not impressive, but does show an expected bulge toward the west associated with a deeper mixed layer that requires excess heating in order to be mixed out. When a negative anomaly of this type is introduced initially, it creates a shallower mixed layer that is advected downstream to create a bulge toward the east by 1800 LT (Fig. 14b). The bulge created in either case is small, suggesting that there is weak convergence. Consistent with this scenario, the mixed-layer peaks are only up to 5 km. Qualitatively the mixed-layer depth anomaly results agree with the topography anomaly results in terms of the direction of the dryline bulge.

The final anomaly considered is a variation in the initial inversion strength with an amplitude $A = 2$ K and a size $\sigma_x = \sigma_y = 200$ km. Again, all model parameters and processes are the same as the benchmark case except that there is a uniform surface heat flux over the domain. Because the inversion strength is inherent to the air, the anomaly changes over time and is advected downstream. Positive and negative anomalies are contrasted in Figs. 13c and 14c. By 1800 LT (Fig. 13c) the amplitude of the anomaly has decreased. However, the dryline bulge that it creates is substantially different than that created by the mixed-layer depth anomaly. An expected bulge toward the west associated with a stronger inversion is seen in Fig. 13c by the 0.5-K inversion strength contour arcing into the bulge. For a weaker inversion the bulge is to the east (Fig. 14c). When there is a strong inversion, the entrainment is less; when there is a weak inversion, the heating is more likely to entrain air into the layer. Consistent with this tendency, the mixed-layer peaks in Fig. 13c are only 4.5 km; those in Fig. 14c are up to 8.5 km.

7. Conclusions

The results of the present mixed-layer study of the dryline extend those of Jones and Bannon (2002) to a two-dimensional geometry that allows for the creation of lateral bulges in the dryline. It has been demonstrated that localized variations in the surface heat flux, topography, inversion strength, and, to a lesser extent, mixed-layer depth are important in the creation of dryline bulges during the day. Depending on the type and sign of the anomaly, the bulges can be either eastward or westward. Due to advection, they typically form downstream of the anomaly center. As the bulge develops, the convergence along the dryline changes, and isolated peaks in the mixed-layer depth appear close to the dryline in the late afternoon. These peaks reach depths of 4 to 9 km and are associated with weak inversions. We speculate that these peaks may be the trigger for the deep

moist convection that develops along the dryline bulges in the afternoon.

At dusk, when the solar forcing of the boundary layer ceases, the steep dryline collapses, and the moist air surges westward several hundred kilometers, and a nocturnal low-level jet forms. The lateral extent of the surge is sensitive to the presence of nocturnal friction. Unlike Jones and Bannon (2002), the present model includes weak surface friction at night (6) and the associated mechanical mixing (10). During the daytime, friction does not induce much of a difference, but at night it slows the westward surge of very shallow fluid (with depths of the order of a centimeter) by up to 200 km. We also note that the inclusion of an isolated anomaly of increased (by 50%) surface drag during the day collocated with the benchmark surface flux anomaly has a negligible impact on the dryline evolution.

As in Jones and Bannon (2002), the nocturnal surge produces a nocturnal eastward propagating mixed-layer gravity wave. The results indicate the wave has a fairly extensive meridional length that is affected by the synoptic winds. Parsons et al. (2000) observed a local elevation in the mixed-layer depth propagating toward the dryline, but this feature was never replicated in the model.

The variety and diversity of the dryline bulges produced in these modeling studies highlight the sensitivity of the dryline to variations in the surface properties of the region and imply the inherent difficulty in forecasting dryline bulges. For example, variations in surface vegetation, soil moisture (and hence previous precipitation), and cloud cover can alter the length, width, and amplitude of a surface-heat-flux anomaly. As a consequence, forecasting the diurnal evolution of the dryline is a challenging boundary layer problem.

Acknowledgments. The National Science Foundation (NSF) under NSF Grants ATM-9729631 and ATM-0215358 provided partial financial support. We thank Jeffrey M. Chagnon and Patrick A. Jones for programming assistance in the early stages of the project.

REFERENCES

Blackadar, A. K., 1957: Boundary layer wind maxima and their significance for the growth of nocturnal inversions. *Bull. Amer. Meteor. Soc.,* **38,** 283–290.

Fujita, T. T., 1958: Structure and movement of a dry front. *Bull. Amer. Meteor. Soc.,* **39,** 574–582.

Grasso, L. D., 2000: A numerical simulation of dryline sensitivity to soil moisture. *Mon. Wea. Rev.,* **128,** 2816–2834.

Jones, P. A., and P. R. Bannon, 2002: A mixed-layer model of the diurnal dryline. *J. Atmos. Sci.,* **59,** 2582–2593.

Keyser, D., and R. A. Anthes, 1977: The applicability of a mixed-layer model of the planetary boundary layer to real-data forecasting. *Mon. Wea. Rev.,* **105,** 1351–1371.

Koch, S. E., 1979: Mesoscale gravity waves as a possible trigger of severe convection along a dryline. Ph.D. dissertation, University of Oklahoma, 195 pp. [Available from UMI, 300 North Zeeb Road, P.O. Box 1346, Ann Arbor, MI 48106-1346.]

McCarthy, J., and S. E. Koch., 1982: The evolution of an Oklahoma dryline. Part I: A meso- and subsynoptic-scale analysis. *J. Atmos. Sci.,* **39,** 225–236.

McNider, R. T., and F. J. Kopp, 1990: Specification of the scale and magnitude of thermals used to initiate convection in cloud models. *J. Appl. Meteor.,* **29,** 99–104.

Miller, J. A., T. A. Kovacs, and P. R. Bannon, 2001: A shallow-water model of the diurnal dryline. *J. Atmos. Sci.,* **58,** 3508–3524.

Parsons, D. B., M. A. Shapiro, and E. Miller, 2000: The mesoscale structure of a nocturnal dryline and of a frontal-dryline merger. *Mon. Wea. Rev.,* **128,** 3824–3838.

Peckham, S. E., and L. J. Wicker, 2000: The influence of topography and lower-tropospheric winds on dryline morphology. *Mon. Wea. Rev.,* **128,** 2165–2189.

Rhea, J. O., 1966: A study of thunderstorm formation along drylines. *J. Appl. Meteor.,* **5,** 58–63.

Schaefer, J. T., 1973: The motion of the dryline. Preprints, *Eighth Conf. on Severe Local Storms,* Denver, CO, Amer. Meteor. Soc. 104–107.

——, 1974a: A simulative model of dryline motion. *J. Atmos. Sci.,* **31,** 956–964.

——, 1974b: The life cycle of the dryline. *J. Appl. Meteor.,* **13,** 444–449.

——, 1986a: The dryline. *Mesoscale Meteorology and Forecasting,* P. S. Ray, Ed., Amer. Meteor. Soc., 549–572.

——, 1986b: Severe thunderstorm forecasting: A historical perspective. *Wea. Forecasting,* **1,** 164–189.

Schär, C., and R. B. Smith, 1993: Shallow water flow past isolated topography. Part I. *J. Atmos. Sci.,* **50,** 1373–1400.

——, and P. K. Smolarkiewicz, 1996: A synchronous and iterative flux-correction formalism for coupled transport equations. *J. Comput. Phys.,* **128,** 101–120.

Shaw, B. L., R. A. Pielke, and C. L. Ziegler, 1997: A three-dimensional numerical simulation of a Great Plains dryline. *Mon. Wea. Rev.,* **125,** 1489–1506.

Stull, R. B., 1988: *An Introduction to Boundary Layer Meteorology.* Kluwer Academic, 666 pp.

Sun, W. Y., and C. C. Wu, 1992: Formation and diurnal variation of the dryline. *J. Atmos. Sci.,* **49,** 1606–1619.

Tennekes, H., 1973: A model for the dynamics of the inversion above a convective boundary layer. *J. Atmos. Sci.,* **30,** 558–567.

Zeman, O., and H. Tennekes, 1977: Parameterization of the turbulent energy budget at the top of the daytime atmospheric boundary layer. *J. Atmos. Sci.,* **34,** 111–123.

Ziegler, C. L., W. J. Martin, R. A. Pielke, and R. Z. Walko, 1995: A modeling study of the dryline. *J. Atmos. Sci.,* **52,** 263–285.